

# Classical dynamics and semiclassical analysis of excitons in cuprous oxide

Jan Ertl,<sup>1</sup> Michael Marquardt,<sup>1</sup> Moritz Schumacher,<sup>1</sup> Patric Rommel,<sup>1</sup> Jörg Main,<sup>1,\*</sup> and Manfred Bayer<sup>2</sup>

<sup>1</sup>*Institut für Theoretische Physik I, Universität Stuttgart, 70550 Stuttgart, Germany*

<sup>2</sup>*Experimentelle Physik 2, Technische Universität Dortmund, 44221 Dortmund, Germany*

(Dated: March 28, 2024)

Excitons, as bound states of electrons and holes, embody the solid state analogue of the hydrogen atom, whose quantum spectrum is explained within a classical framework by the Bohr–Sommerfeld atomic model. In a first hydrogenlike approximation the spectra of excitons are also well described by a Rydberg series, however, due to the surrounding crystal environment deviations from this series can be observed. A theoretical treatment of excitons in cuprous oxide needs to include the band structure of the crystal, leading to a prominent fine-structure splitting in the quantum spectra. This is achieved by introducing additional spin degrees of freedom into the system, making the existence and meaningfulness of classical exciton orbits in the physical system a non-trivial question. Recently, we have uncovered the contributions of periodic exciton orbits directly in the quantum mechanical recurrence spectra of cuprous oxide [J. Ertl *et al.*, Phys. Rev. Lett. **129**, 067401 (2022)] by application of a scaling technique and fixing the energy of the classical dynamics to a value corresponding to a principle quantum number  $n = 5$  in the hydrogenlike case. Here, we present a comprehensive derivation of the classical and semiclassical theory of excitons in cuprous oxide. In particular, we investigate the energy dependence of the exciton dynamics. Both the semiclassical and quantum mechanical recurrence spectra exhibit stronger deviations from the hydrogenlike behavior with decreasing energy, which is related to a growing influence of the spin-orbit coupling and thus a higher velocity of the secular motion of the exciton orbits. The excellent agreement between semiclassical and quantum mechanical exciton recurrence spectra demonstrates the validity of the classical and semiclassical approach to excitons in cuprous oxide.

## I. INTRODUCTION

Since the early days of quantum mechanics and the development of Bohr’s model for the hydrogen atom there has been a long standing debate on the significance of classical dynamics in quantum theory. The states of the hydrogen atom can well be described by application of the semiclassical Bohr–Sommerfeld quantization rules [1], however, the old quantum theory already fails for the computation of the ground state energy of the helium atom with its underlying classically chaotic three-body dynamics. Modern semiclassical theories for both regular and chaotic multidimensional systems have been derived in the 1970’s; Gutzwiller’s periodic-orbit theory [2] describes the density of states of chaotic systems in terms of periodic-orbit parameters of the underlying classical system, an analogous theory has been developed by Berry and Tabor for integrable systems [3]. The semiclassical trace formulas of these theories are the foundation for, e.g., the physical interpretation of quantum spectra of the diamagnetic Kepler problem [4–6], the helium atom [7], and the application of random matrix theory to the quantum spectra of classically chaotic systems [8].

A system similar to the hydrogen atom occurs in solid state physics. When an electron is excited from the valence band of a semiconductor to the conduction band it leaves behind a positively charged hole in the valence band. Due to the Coulomb interaction between electron and hole the two particles can form a bound hydrogen-

like state, called exciton. While semiclassical approaches are now well established in atomic physics, the majority of theoretical investigations on excitons are performed within a quantum mechanical framework [9–13]. This might be due to historical reasons; when first discovered in 1956 only exciton states with low principle quantum numbers were experimentally accessible [14]. This situation has changed in 2014 when Kazimierzczuk *et al.* observed giant Rydberg excitons up to principle quantum numbers  $n = 25$  in cuprous oxide [15]. Recently even Rydberg excitons with quantum numbers up to  $n = 30$  could be resolved [16]. Taking into account the material parameters of cuprous oxide the size of these states is of the order of several  $\mu\text{m}$ , and thus the classical correspondence principle should be applicable.

The question whether or not the quantum mechanical exciton spectra can be explained in terms of a classical exciton dynamics is nontrivial and interesting due to the fact that the experimental spectra of cuprous oxide are far more complicated than hydrogenlike Rydberg spectra. In particular, the exciton spectra exhibit a prominent fine-structure splitting [11]. In the quantum computations this fine structure can be considered by introducing additional spin degrees of freedom, viz. a quasispin  $I$ , which couples to the spin  $S_h$  of the holes in the valence band [12, 17, 18]. To obtain a classical picture an adiabatic approach can be applied, where the spin degrees of freedom are treated in a quantum mechanical framework, while the relative coordinates and momenta are considered as classical variables [19].

A semiclassical analysis of quantum spectra is possible by extracting the periodic orbit parameters of the

\* Email: main@itp1.uni-stuttgart.de

underlying classical dynamics by using the semiclassical trace formulas, which describe the density of states as a superposition of sinusoidal contributions from periodic orbits [2, 3]. This is most easy for systems possessing a scaling property in a way that the classical dynamics does not depend on the energy or a suitable scaling parameter [6]. Contrary to hydrogenlike systems, which become energy-independent by application of an appropriate scaling transformation [6], the dynamics of excitons in cuprous oxide, due to the spin-orbit coupling, still depends on the energy, however, a scaling property can be recovered via a modification of the spin-orbit term [20]. The Fourier transform of the quantum mechanical density of states then yields quantum mechanical recurrence spectra with peaks corresponding to actions of periodic exciton orbits. In Ref. [20] we demonstrated the existence of classical exciton orbits in the recurrence spectra of a system where the energy for the classical dynamics is fixed to a value corresponding to a principle quantum number  $n = 5$  in the hydrogenlike case.

In this paper we derive the classical and semiclassical theory for excitons in cuprous oxide. We discuss the energy dependence of classical exciton orbits and demonstrate the resulting differences in the corresponding recurrence spectra. In Sec. II we present the Hamiltonian for excitons in cuprous oxide. The adiabatic approach leading to a classical description of excitons and the resulting classical dynamics are discussed in Sec. III. Here we study the energy dependence of the phase space structure via Poincaré surfaces of section (PSOS) of orbits in the two distinct symmetry planes. Furthermore, we discuss stability properties of periodic orbits, as well as the organization of the action for one- to three-dimensional periodic orbits. The relation of classical exciton orbits to the quantum properties of the crystal can be established by semiclassical methods. The techniques used in this manuscript are presented in Sec. IV as well as the calculation scheme of semiclassical amplitudes. The semiclassical results are then compared to quantum mechanical calculations. In Sec. V we introduce the techniques used for the solution of the quantum mechanical problem, and present a detailed comparison of semiclassical amplitudes and quantum recurrence spectra. An outlook and conclusion are given in Sec. VI.

## II. EXCITONS IN CUPROUS OXIDE

Excitons in a semiconductor like cuprous oxide are excitations of the crystal, where an electron is lifted from one of the valence bands to the conduction band, leaving behind a hole. In a simple model, i.e., neglecting the valence band structure, the electron and hole, due to the Coulomb interaction, can form bound states similar to the Rydberg series in the hydrogen atom. The complex valence band structure of cuprous oxide causes fine-structure splittings in the spectra, which can be considered via correction terms to the kinetic energy that

break the spherical symmetry. In the case of excitons in cuprous oxide, these terms originate from the non-parabolic shape of the uppermost valence bands, which belong to the irreducible representation  $\Gamma_5^+$  [9, 10] of the cubic  $O_h$  symmetry group [21] of the crystal. The treatment of the three-dimensional space of Bloch functions leads to the introduction of auxiliary degrees of freedom compared to the hydrogenlike model, i.e., the quasispin  $\mathbf{I}$  in addition to the hole spin  $\mathbf{S}_h$ , whose components are given by the spin matrices for  $I = 1$  and  $S_h = 1/2$ , respectively [22–24]. The excitons in cuprous oxide can be described using the Hamiltonian [12]

$$H = E_g + H_e(\mathbf{p}_e) + H_h(\mathbf{p}_h, \hat{\mathbf{I}}, \hat{\mathbf{S}}_h) - \frac{e^2}{4\pi\epsilon_0\epsilon|\mathbf{r}_e - \mathbf{r}_h|}. \quad (1)$$

Here,

$$H_e(\mathbf{p}_e) = \frac{1}{2m_e}\mathbf{p}_e^2 \quad (2)$$

and

$$\begin{aligned} H_h(\mathbf{p}_h, \hat{\mathbf{I}}, \hat{\mathbf{S}}_h) = & \frac{\gamma_1}{2m_0}\mathbf{p}_h^2 + \frac{1}{2\hbar^2m_0}[4\gamma_2\hbar^2\mathbf{p}_h^2 \\ & - 6\gamma_2(p_{h1}^2\mathbf{I}_1^2 + \text{c.p.}) - 12\gamma_3(\{p_{h1}, p_{h2}\}\{\mathbf{I}_1, \mathbf{I}_2\} + \text{c.p.}) \\ & - 12\eta_2(p_{h1}^2\mathbf{I}_1\mathbf{S}_{h1} + \text{c.p.}) + 2(\eta_1 + 2\eta_2)\mathbf{p}_h^2(\mathbf{I} \cdot \mathbf{S}_h) \\ & - 12\eta_3(\{p_{h1}, p_{h2}\}(\mathbf{I}_1\mathbf{S}_{h2} + \mathbf{I}_2\mathbf{S}_{h1}) + \text{c.p.})] + H_{\text{SO}} \quad (3) \end{aligned}$$

are the kinetic energy of the electron and hole at positions  $\mathbf{r}_e$  and  $\mathbf{r}_h$  with momentum  $\mathbf{p}_e$  and  $\mathbf{p}_h$ , respectively.  $\{a, b\} = \frac{1}{2}(ab + ba)$  denotes the symmetrized product, c.p. stands for cyclic permutation, and  $\gamma_i$  and  $\eta_i$  are the Luttinger parameters. Eq. (2) differs from the kinetic energy in the vacuum only by a modified electron mass  $m_e$ , i.e., the conduction band remains a parabola. By contrast, the degenerate  $\Gamma_5^+$  bands significantly deviate from a parabolic shape. The terms in Eq. (3) form the Suzuki-Hensel Hamiltonian [24], which includes all corrections up to quadratic order in  $\mathbf{p}_h$  that are compatible with the  $O_h$  symmetry of the crystal. The degrees of freedom of the hole in the  $\Gamma_5^+$  bands can be described by an effective internal angular momentum, viz. the quasispin  $\mathbf{I}$ . The last term in Eq. (1) is the screened Coulomb potential with the dielectric constant  $\epsilon$ . In this work we neglect central-cell corrections, which play a role for the even exciton states only and have been studied in detail in Refs. [13, 25, 26].

When the system is expressed in relative and center-of-mass coordinates [27],

$$\begin{aligned} \mathbf{r} &= \mathbf{r}_e - \mathbf{r}_h, & \mathbf{R} &= \frac{m_h\mathbf{r}_h + m_e\mathbf{r}_e}{m_h + m_e}, \\ \mathbf{P} &= \mathbf{p}_e + \mathbf{p}_h, & \mathbf{p} &= \frac{m_h\mathbf{p}_e - m_e\mathbf{p}_h}{m_h + m_e}, \end{aligned} \quad (4)$$

with vanishing center-of-mass momentum  $\mathbf{P} = 0$ , we obtain the Hamiltonian [12, 17, 18]

$$H = E_g + H_{\text{kin}}(\mathbf{p}, \mathbf{I}, \mathbf{S}_h) - \frac{e^2}{4\pi\epsilon_0\epsilon|\mathbf{r}|} + H_{\text{SO}}. \quad (5)$$

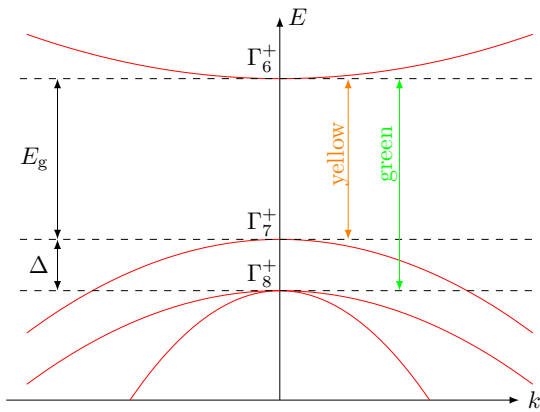


FIG. 1. Schematic view of the band structure. The conduction band belongs to irreducible representation  $\Gamma_6^+$  while at the  $\Gamma$ -point a  $\Gamma_7^+$  and  $\Gamma_8^+$  valence band exists. These bands are separated by the spin-orbit coupling  $\Delta$ . Transitions from the upper and lower valence band to the conduction band result in the yellow and green exciton series, respectively.

Here the second term,

$$\begin{aligned}
 H_{\text{kin}}(\mathbf{p}, \mathbf{I}, \mathbf{S}_h) = & \frac{\gamma'_1}{2m_0} \mathbf{p}^2 + \frac{1}{2\hbar^2 m_0} [4\gamma_2 \hbar^2 \mathbf{p}^2 \\
 & - 6\gamma_2 (p_1^2 \mathbf{I}_1^2 + \text{c.p.}) - 12\gamma_3 (\{p_1, p_2\} \{\mathbf{I}_1, \mathbf{I}_2\} + \text{c.p.}) \\
 & - 12\eta_2 (p_1^2 \mathbf{I}_1 \mathbf{S}_{h1} + \text{c.p.}) + 2(\eta_1 + 2\eta_2) \mathbf{p}^2 (\mathbf{I} \cdot \mathbf{S}_h) \\
 & - 12\eta_3 (\{p_1, p_2\} (\mathbf{I}_1 \mathbf{S}_{h2} + \mathbf{I}_2 \mathbf{S}_{h1}) + \text{c.p.})], \quad (6)
 \end{aligned}$$

accounts for the kinetic energy of the electron and hole quadratic in the momentum  $\mathbf{p}$ , with  $\gamma'_1 = \gamma_1 + m_0/m_e$ . Additionally, the Suzuki-Hensel Hamiltonian (3) contains a spherically-symmetric term that couples the quasispin and hole spin, viz. the spin-orbit term

$$H_{\text{SO}} = \frac{2}{3} \Delta \left( 1 + \frac{1}{\hbar^2} \mathbf{I} \cdot \mathbf{S}_h \right). \quad (7)$$

Here,  $\Delta$  denotes the spin-orbit coupling strength. This leads to a splitting of the  $\Gamma_5^+$  band into a higher lying two-fold degenerate  $\Gamma_7^+$  band, connected to the yellow exciton series, and a lower lying four-fold degenerate  $\Gamma_8^+$  band, connected to the green exciton series [9, 10, 21]. A schematic of the band structure is shown in Fig. 1. The first term in the Hamiltonian (1) is the band-gap energy  $E_g$  between the uppermost  $\Gamma_7^+$  valence band and the lowermost  $\Gamma_6^+$  conduction band as also illustrated in Fig. 1. The material parameters of cuprous oxide are given in Table I.

### III. CLASSICAL EXCITON DYNAMICS

The classical exciton dynamics of the simple hydrogen-like model with Hamiltonian

$$H_{\text{hyd}} = E_g + \frac{\gamma'_1}{2m_0} \mathbf{p}^2 - \frac{e^2}{4\pi\epsilon_0\epsilon|\mathbf{r}|}, \quad (8)$$

is well known. The bound orbits are classical Kepler ellipses, which are obtained as analytical solutions of Hamilton's equations of motion. For the Hamiltonian (8) the scaling

$$\mathbf{r} = n_{\text{eff}}^2 \tilde{\mathbf{r}}, \quad \mathbf{p} = \frac{1}{n_{\text{eff}}} \tilde{\mathbf{p}}, \quad (9)$$

of the coordinates and momenta with the effective quantum number  $n_{\text{eff}} \equiv \sqrt{E_{\text{Ryd}}/(E_g - E)}$ , where  $E_{\text{Ryd}}$  is the exciton Rydberg energy, removes the energy dependence from the Hamiltonian after multiplication with  $n_{\text{eff}}^2$ . This means that, up to a scaling of the Kepler ellipses, the classical dynamics is the same at all energies. The situation, however, becomes more complicated when considering the full Hamiltonian (5). The additional band structure terms

$$\begin{aligned}
 H_{\text{band}}(\mathbf{p}, \mathbf{I}, \mathbf{S}_h) = & \frac{1}{2\hbar^2 m_0} [4\gamma_2 \hbar^2 \mathbf{p}^2 \\
 & - 6\gamma_2 (p_1^2 \mathbf{I}_1^2 + \text{c.p.}) - 12\gamma_3 (\{p_1, p_2\} \{\mathbf{I}_1, \mathbf{I}_2\} + \text{c.p.}) \\
 & - 12\eta_2 (p_1^2 \mathbf{I}_1 \mathbf{S}_{h1} + \text{c.p.}) + 2(\eta_1 + 2\eta_2) \mathbf{p}^2 (\mathbf{I} \cdot \mathbf{S}_h) \\
 & - 12\eta_3 (\{p_1, p_2\} (\mathbf{I}_1 \mathbf{S}_{h2} + \mathbf{I}_2 \mathbf{S}_{h1}) + \text{c.p.})] + H_{\text{SO}}, \quad (10)
 \end{aligned}$$

which are neglected in the hydrogenlike model (8), depend on the additional degrees of freedom introduced by the quasispin  $\mathbf{I}$  and the hole spin  $\mathbf{S}_h$ . Note that the spin-orbit term  $H_{\text{SO}}$  given in Eq. (7) disables the scaling procedure described above to remove the energy dependence of the Hamiltonian (5).

#### A. Adiabatic approach

To obtain classical exciton orbits and their parameters from the Hamiltonian (5) the spin degrees of freedom

TABLE I. Material parameters of  $\text{Cu}_2\text{O}$  used in this paper.

band-gap energy	$E_g$	2.172 08 eV	[15]
electron mass	$m_e$	$0.99m_0$	[28]
hole mass	$m_h$	$0.58m_0$	[28]
dielectric constant	$\epsilon$	7.5	[29]
spin-orbit coupling	$\Delta$	0.131 eV	[10]
Luttinger parameters	$\gamma_1$	1.76	[10]
	$\gamma_2$	0.7532	[10]
	$\gamma_3$	-0.3668	[10]
	$\eta_1$	-0.02	[10]
	$\eta_2$	-0.00367	[10]
	$\eta_3$	-0.03367	[10]

also need to be considered. Therefore, we resort to the adiabatic approach introduced in Ref. [19]. The idea is based on the different characteristic timescales, related to the corresponding energy splittings  $T \sim \hbar/\Delta E$ , on which the dynamics of the spin degrees of freedom and the relative coordinates take place. While for the Rydberg series the splittings  $\Delta E \sim 2E_{\text{Ryd}}/n^3$  strongly decrease with increasing quantum number  $n$ , the spin-orbit splitting caused by the spin degrees of freedom is fixed to the value of the spin-orbit coupling  $\Delta$ . Comparing the values of  $E_{\text{Ryd}}$  and  $\Delta$  it becomes apparent that the dynamics of the spin degrees of freedom becomes much faster than the dynamics of the relative motion already for quantum numbers  $n \gtrsim 3$ . This means that the spin degrees of freedom can react almost instantly to changes in the relative configuration of the coordinates. Thus we consider the spin degrees of freedom quantum mechanically by diagonalizing the band-structure part of the Hamiltonian (10) in a six-dimensional basis for the quasispin and hole spin  $|m_I, m_{S_h}\rangle$  with the corresponding magnetic quantum numbers  $m_I$  and  $m_{S_h}$ . This yields three distinct two-fold degenerate energy surfaces  $W_k(\mathbf{p})$  in momentum space obeying the eigenvalue equation

$$H_{\text{band}}(\mathbf{p}, \mathbf{I}, \mathbf{S}_h)\chi_k(\mathbf{p}; \mathbf{I}, \mathbf{S}_h) = W_k(\mathbf{p})\chi_k(\mathbf{p}; \mathbf{I}, \mathbf{S}_h) \quad (11)$$

with the corresponding wave functions

$$\chi_k(\mathbf{p}; \mathbf{I}, \mathbf{S}_h) = \sum_{m_I, m_{S_h}} c_{m_I, m_{S_h}}(\mathbf{p}) |m_I, m_{S_h}\rangle, \quad (12)$$

which can be assigned to the different exciton series, i.e., one for the yellow series and two for the green series. The two-fold degeneracies can be explained using Kramers' theorem. Note that this procedure is somehow the inverse of fitting the Luttinger parameters  $\gamma_i$  and  $\eta_i$  to energy surfaces obtained from spin-DFT calculations [9, 10]. The adiabatic approach can now be derived by using the product ansatz

$$\Psi = \sum_k \Phi_k(\mathbf{p})\chi_k(\mathbf{p}; \mathbf{I}, \mathbf{S}_h) \quad (13)$$

in momentum space. Inserting this ansatz into the full Hamiltonian (5) and multiplication from the left with  $\chi_{k'}$  yields six equations

$$\mathcal{H}\Phi = \left[ \left( E_g + \frac{\gamma'_1}{2m_0} \mathbf{p}^2 + W_k(\mathbf{p}) \right) \delta_{k'k} + \mathcal{H}_C \right] \Phi = E\Phi, \quad (14)$$

where the operator  $\mathcal{H}_C$ , defined as

$$(\mathcal{H}_C)_{k'k} = \langle \chi_{k'} | \frac{-e^2}{4\pi\epsilon_0\epsilon|\mathbf{r}|} | \chi_k \rangle, \quad (15)$$

couple the different wave functions  $\Phi_k$ . However, for Rydberg excitons with quantum numbers  $n \gtrsim 3$  the coupling terms can be neglected because of the different time scales of the spin degrees and the relative motion as explained above, which leads to the Schrödinger equation

$$\left[ E_g + \frac{\gamma'_1}{2m_0} \mathbf{p}^2 - \frac{e^2}{4\pi\epsilon_0\epsilon|\mathbf{r}|} + W_k(\mathbf{p}) \right] \Phi_k = E\Phi_k. \quad (16)$$

In this work we restrict the analysis of the exciton dynamics to the yellow series described by the classical Hamilton function

$$\mathcal{H} = E_g + \frac{\gamma'_1}{2m_0} \mathbf{p}^2 - \frac{e^2}{4\pi\epsilon_0\epsilon|\mathbf{r}|} + W_{1,2}(\mathbf{p}) = E, \quad (17)$$

with the two-fold degenerate lowest pair of energy surfaces  $W_{1,2}(\mathbf{p})$ . Since the Hamilton function (17) only depends on the relative coordinates  $\mathbf{r}$  and  $\mathbf{p}$  we obtain classical exciton orbits by fixing the energy  $E = E_g - E_{\text{Ryd}}/n_{\text{eff}}^2$ , i.e., using a fixed value  $n_{\text{eff}} = n_0$ , and then numerically integrating Hamilton's equations of motion

$$\dot{r}_i = \frac{\gamma'_1}{m_0} p_i + \frac{\partial W_k(\mathbf{p})}{\partial p_i}, \quad \dot{p}_i = -\frac{e^2}{4\pi\epsilon_0\epsilon} \frac{r_i}{|\mathbf{r}|^3}, \quad (18)$$

with, e.g., a standard Runge-Kutta algorithm [30]. Due to the additional band structure terms carried by the energy surfaces  $W_k$  the spherical SO(4) symmetry of the hydrogenlike problem is reduced to the cubic  $O_h$  symmetry. For the cubic symmetry nine symmetry planes exist, where a two-dimensional motion is possible. One can distinguish two classes of symmetry planes. The three planes normal to the [100] axis and its equivalents exhibit the same dynamics and likewise the six planes normal to the  $[1\bar{1}0]$  axis and its equivalents. In contrast to the hydrogenlike model where every starting configuration leads to a two-dimensional orbit, three-dimensional orbits are possible when moving the starting configurations out of the symmetry planes. This leads to an intricate phase space structure for excitons in cuprous oxide.

## B. Classical exciton orbits and PSOS

Since the phase space of the classical exciton dynamics described by the Hamiltonian (17) is six-dimensional it cannot easily be visualized. However, the phase space related to the two-dimensional orbits in the symmetry planes normal to the [100] and  $[1\bar{1}0]$  axes can be analyzed directly by looking at the corresponding PSOS. They are constructed by choosing a two-dimensional hyperplane in the four-dimensional phase space, here the  $(z, p_z)$  plane, and recording the intersection points of orbits when crossing the  $z$  axis, i.e.,  $x = y = 0$ . The remaining momenta  $p_x$  and  $p_y$  are given by the conservation of energy and the choice of the symmetry plane. Such PSOS are shown in Fig. 2 for the two different symmetry planes and three different values of  $n_0$ . In general, the PSOS exhibit regular, i.e., integrable or near-integrable parts of the phase space as toruslike regular structures, while chaotic motion is indicated by stochastic regions. Periodic orbits appear as fixed points in the PSOS.

In all PSOS in Fig. 2 one can observe a central fixed point, belonging to a nearly circular orbit shown as inset in the bottom right of the PSOS. This orbit is surrounded by regular tori, which cover the majority of phase space.

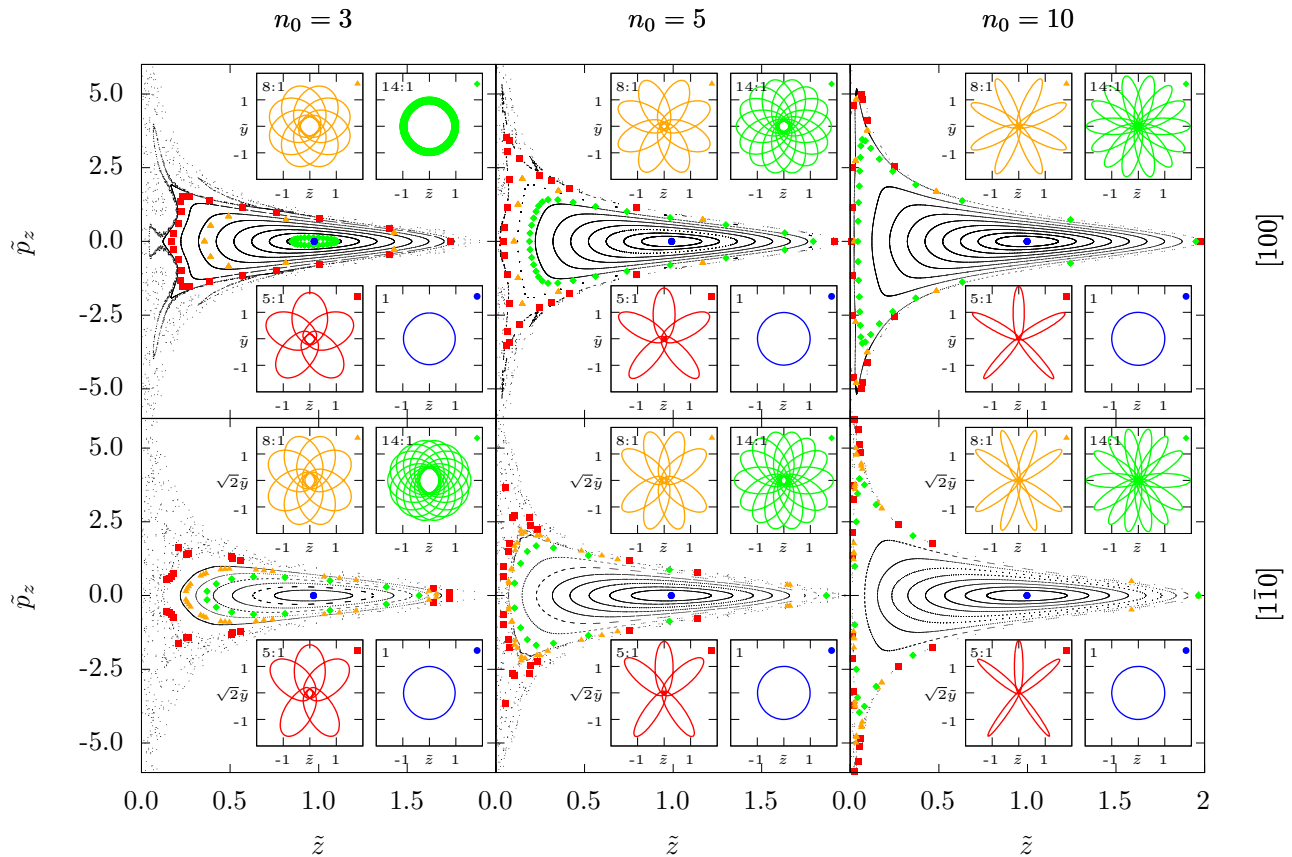


FIG. 2. PSOS for the symmetry planes normal to  $[100]$  (top row) and normal to  $[1\bar{1}0]$  (bottom row) at  $n_0 = 3$  (left),  $n_0 = 5$  (middle), and  $n_0 = 10$  (right). A selection of orbits is shown as insets, labeled by their winding numbers  $M_1 = 1$  for the nearly circular orbits and  $M_1:M_2$  for the periodic orbits on the two-dimensional tori. Their positions in the PSOS are marked by corresponding symbols. Coordinates and momenta are given in the scaled units (9) and thus approximately cover the same range for all values of  $n_0$ . The figure extends previous results for  $n_0 = 5$  in the plane  $\perp [100]$  presented in Ref. [19].

The outermost parts of the PSOS exhibit small stochastic (chaotic) regions. The area of the chaotic region is larger for the symmetry plane normal to  $[1\bar{1}0]$  and decreases with increasing values of  $n_0$ . In the regular, near-integrable regions the two-dimensional orbits are characterized as a secular motion of Kepler ellipses. Here, stable and unstable periodic orbits appear in pairs of elliptic and hyperbolic fixed points in accordance with the Poincaré–Birkhoff theorem as illustrated in the enlarged PSOS in Fig. 3. These periodic orbits can be classified by two integer winding numbers  $M_1$  and  $M_2$  with  $M_1$  the number of Kepler ellipses and  $M_2$  the number of circulations on the torus caused by the secular motion until repetition. Some of them are illustrated in Fig. 3 and as insets in Fig. 2. The assignment of winding numbers can be confirmed by Fourier analysis of the periodic orbit coordinate functions [31, 32]. The ratio  $M_1/M_2$  of the winding numbers increases when moving from the outermost part of the PSOS towards the central fixed point, where it takes its maximum value. This is related to a decrease of the eccentricity of the Kepler ellipses and thus to an increase of the angular momentum vector in

the direction perpendicular to the symmetry plane. The maximum ratio  $(M_1/M_2)_{\max}$  is larger in the symmetry plane normal to  $[1\bar{1}0]$  and increases with increasing  $n_0$ . It is important to note that the speed of the secular motion strongly decreases with growing  $n_0$  and thus with growing energy. As can be seen in Fig. 2 tori with the same ratio  $M_1/M_2$  of the winding numbers are shifted towards the outer regions of the PSOS with increasing  $n_0$ , which means that the inner regions more and more belong to tori with higher ratios  $M_1/M_2$  related to orbits with slower secular motion, i.e., the band structure of the crystal has a stronger influence on states with low principal quantum numbers and a lower influence on highly excited Rydberg excitons. Furthermore, orbits in the two distinct symmetry planes also differ in their symmetry properties and their orbit parameters.

The exciton dynamics outside the symmetry planes is characterized by three-dimensional orbits, where a secular motion of Kepler ellipses occurs in orientations described by two angles  $\vartheta$  and  $\varphi$ . Here, periodic orbits can be classified by three winding numbers, where the third winding number  $M_3$  counts the cycles of the sec-

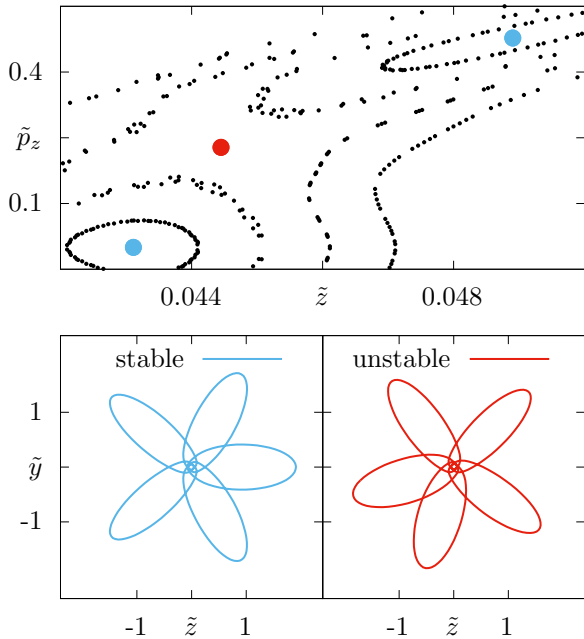


FIG. 3. Top: Enlarged part of the PSOS for the plane normal to  $[100]$  at  $n_0 = 5$ , where two fixed points are surrounded by elliptic and hyperbolic structures, respectively. Bottom: Stable and unstable periodic orbit with winding numbers  $M_1:M_2 = 5:1$  corresponding to the two fixed points.

ular motion in the additional direction compared to the two-dimensional case. The orbits appear in sets of four distinguished variants, not counting rotations and reflections of the same orbit within the  $O_h$  symmetry group. A quadruple of three-dimensional orbits with  $n_0 = 5$  and winding numbers  $M_1:M_2:M_3 = 16:1:2$  is illustrated in Fig. 4. The projection of the three-dimensional orbits onto the  $yz$  plane looks similar to the corresponding two-dimensional orbits, where the orbits in the same column show comparable behavior. The orbits in the same row have identical orientation towards a symmetry plane of the crystal. The orbits in the upper row appear folded towards the plane normal  $[001]$ , whereas the orbits in the lower row are oriented towards the plane normal to  $[0\bar{1}1]$ .

### C. Stability properties of periodic orbits

The application of semiclassical periodic orbit theories in the following sections requires the computation of periodic orbit parameters, including a quantitative description of their stability properties. The stability matrix  $\mathbf{M}(T)$  describes, in a linear approximation, the deviation of the phase space vector

$$\gamma(t) = \begin{pmatrix} \mathbf{r}(t) \\ \mathbf{p}(t) \end{pmatrix} \quad (19)$$

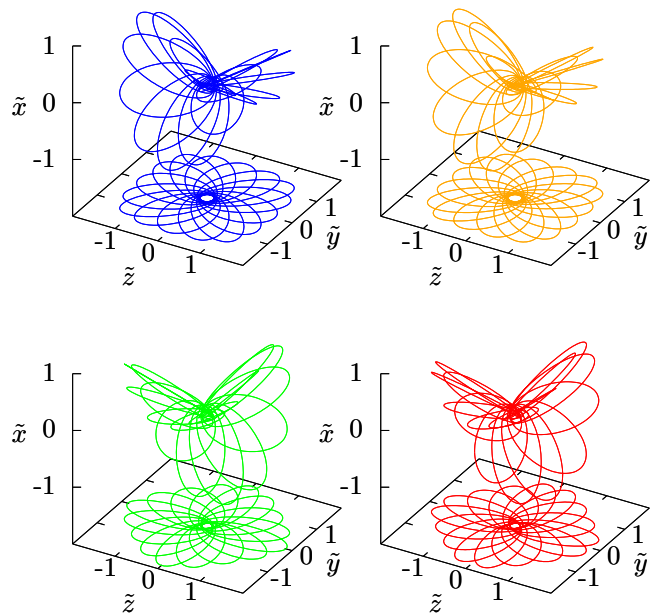


FIG. 4. Three-dimensional orbits with winding numbers  $M_1:M_2:M_3 = 16:1:2$ . Four distinct orbits with different orientation and position of their maxima exist. The projection onto the  $yz$ -plane is shown below each orbit.

from the initial point  $\gamma(0)$  after one period, i.e.,

$$\Delta\gamma(T) = \mathbf{M}(T)\Delta\gamma(0), \quad (20)$$

and can be calculated by integrating

$$\frac{d}{dt}\mathbf{M} = \mathbf{J} \frac{\partial^2 H}{\partial \gamma \partial \gamma} \mathbf{M}, \quad \text{with } \mathbf{J} = \begin{pmatrix} \mathbf{0} & \mathbf{1} \\ -\mathbf{1} & \mathbf{0} \end{pmatrix} \quad (21)$$

and  $\mathbf{M}(0) = \mathbf{1}$  along the corresponding orbit.

Since the stability matrix is symplectic the eigenvalues appear in pairs  $\lambda_i$  and  $1/\lambda_i$ . An absolute value of the sum  $|\lambda_i + 1/\lambda_i| > 2$  indicates that the corresponding direction is unstable, while values  $|\lambda_i + 1/\lambda_i| \leq 2$  indicate a stable direction. For every constant of motion a pair of eigenvalues  $\lambda_i = 1$  does exist. The stability eigenvalues also allow us to study the stability properties of two-dimensional orbits out of the symmetry planes.

For the nearly circular orbits the values of  $\lambda_i + 1/\lambda_i$  as functions of  $n_0$  are shown in Fig. 5. For both orbits the stability in the symmetry plane (red and green curves) is almost identical. For the direction out of the plane the behavior differs. The nearly circular orbit in the plane normal to  $[100]$  is stable and the orbit normal to  $[1\bar{1}0]$  is unstable against perturbations out of the symmetry planes. For the two-dimensional orbits a similar behavior can be observed. Orbits in the plane normal to  $[1\bar{1}0]$  are unstable against perturbations of the orbits out of the plane, whereas the orbits in the symmetry plane normal to  $[100]$  are mostly stable. This can be seen in Fig. 6, where the sums  $\lambda_i + 1/\lambda_i$  for the directions orthogonal

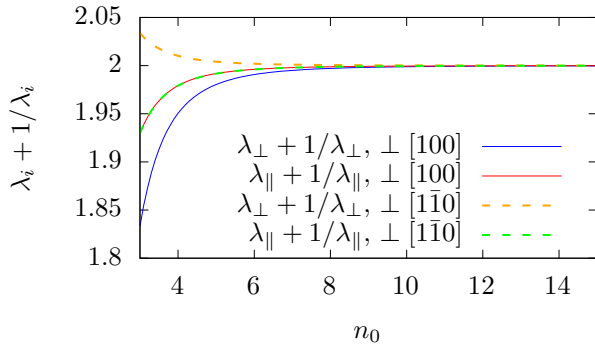


FIG. 5. Sum  $\lambda_i + 1/\lambda_i$  for the nearly circular orbits in the different symmetry planes, where  $\lambda_{\parallel}$  and  $\lambda_{\perp}$  describe the stability of the orbits in the plane and out of the plane, respectively. The directions normal to the symmetry plane are stable for the plane normal to  $[100]$  (blue curve) and unstable for the plane normal to  $[1\bar{1}0]$  (orange curve). Both orbits are stable with respect to perturbations in the plane with almost identical stability eigenvalues  $\lambda_{\parallel}$  (red and green curves).

to the orbit are shown for  $n_0 = 3, 5$ , and  $10$ . Regarding perturbations within the symmetry plane for a given ratio  $M_1/M_2$  two partner orbits exist, one stable and one unstable, as already discussed above (see the elliptic and hyperbolic fixed points in Fig. 3). The largest deviation from  $\lambda_{\parallel} = 1$  is found at low ratios  $M_1/M_2$ , where the influence of the band structure terms on the orbits becomes more pronounced. The strongest effect occurs for orbits exhibiting high symmetry, which are the shortest orbits in the fundamental region.

The stability eigenvalues of the two orbits with the same ratio  $M_1/M_2$  against perturbations out of the symmetry plane are nearly identical and mostly located in the stable region, i.e.,  $|\lambda_{\perp} + 1/\lambda_{\perp}| \leq 2$ . However, for the stability properties in the symmetry plane only the orbits with a low ratio  $M_1/M_2$  show deviations from the integrable behavior characterized by  $\lambda_{\parallel} = 1$  and for  $n_0 = 3$  no deviations can be observed at all. We observe a similar behavior for the periodic orbits in the other symmetry plane and for the three-dimensional orbits.

#### D. Action and ordering scheme for orbits in cuprous oxide

To connect the classical trajectories to quantum properties of the system the action  $S$  of classical orbits is needed. It can be calculated by integrating the corresponding equation of motion

$$\frac{d}{dt}S = \mathbf{p} \frac{d\mathbf{r}}{dt} \quad (22)$$

along the orbit. In Fig. 7 the difference of the action to the one of two-dimensional orbits in the plane normal to  $[100]$  normalized by the second winding number  $M_2$  is plotted over the ratio  $M_1/M_2$  of the first two winding

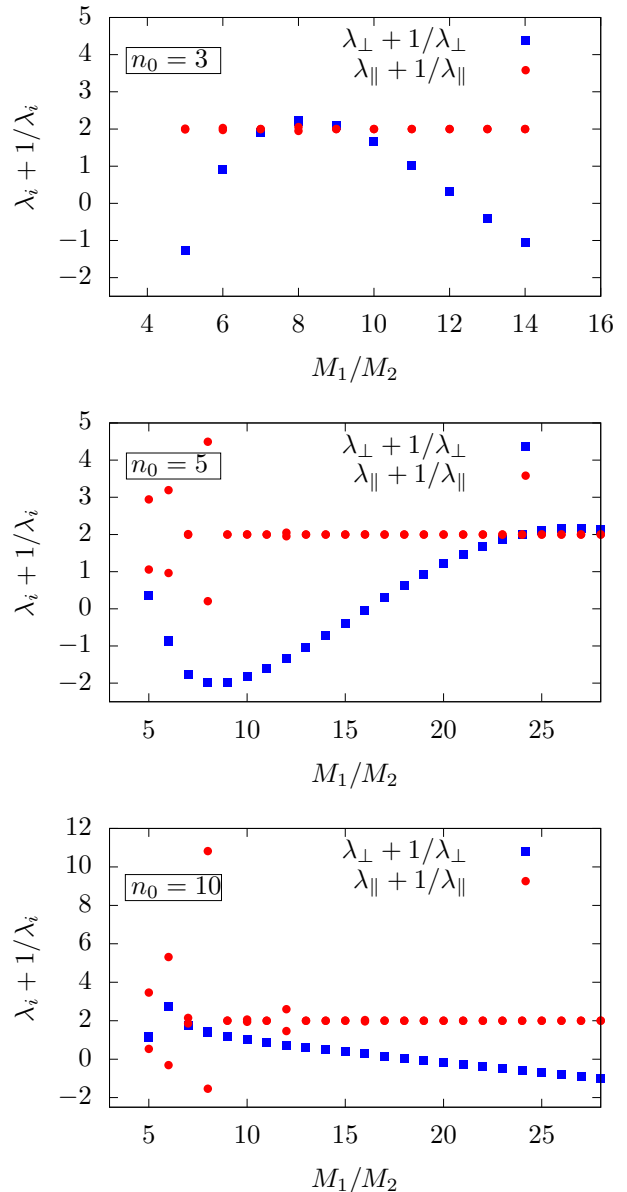


FIG. 6. Sum  $\lambda_i + 1/\lambda_i$  for the two-dimensional orbits in the plane normal to  $[100]$  for  $n_0 = 3$  (top),  $n_0 = 5$  (middle), and  $n_0 = 10$  (bottom).  $\lambda_{\parallel}$  describes the stability of the orbits in the plane,  $\lambda_{\perp}$  describes the stability of the orbits out of the plane. The stability eigenvalues for  $n_0 = 3$  and  $10$  extend results presented for  $n_0 = 5$  in the Supplemental Material of Ref. [20].

numbers at  $n_0 = 5$  for selected pairs of winding numbers  $M_2:M_3$ . Different values of  $n_0$  lead to qualitatively similar pictures. Note that additional orbits with other pairs of winding numbers  $M_2:M_3$  would fill a finite dense area in Fig. 7. With increasing ratio  $M_1/M_2$  the three-dimensional orbits approach the zero line, where the two-dimensional orbits are located and disappear when this line is reached. The ratio  $M_1/M_2$  where this is happening for the orbits with  $M_2:M_3 = 1:2$  corresponds to the

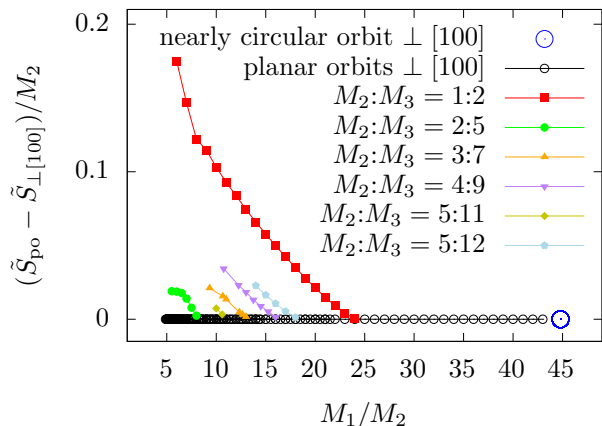


FIG. 7. Difference of the action  $\tilde{S}_{\text{po}}$  of the periodic orbits (po) at  $n_0 = 5$  and the corresponding two-dimensional orbits  $\tilde{S}_{\perp[100]}$  in the plane normal to  $[100]$  normalized by their winding number  $M_2$  over the ratio of winding numbers  $M_1/M_2$ . Six different series of three-dimensional orbits with winding numbers  $M_2:M_3$  are shown as solid points, connected by lines to guide the eye. The action of two-dimensional orbits in the plane normal to  $[100]$  provides a lower border for the families of three-dimensional orbits. For increasing ratio  $M_1/M_2$  the nearly circular orbit (indicated by a blue circle) is reached.

region in Fig. 6 where  $|\lambda_i + 1/\lambda_i| \rightarrow 2$ . A crossing of the line  $|\lambda_i + 1/\lambda_i| = 2$  indicates a change of stability properties, which is connected to a bifurcation of the respective orbit. Similarly, the eigenvalues of two-dimensional orbits with higher values of  $M_2$  approach  $\lambda_i = 1$  where the corresponding three-dimensional orbits disappear. Thus, the two-dimensional orbits constitute a boundary for the three-dimensional orbits. For increasing values of the ratio  $M_1/M_2$  these orbits approach the action of the nearly circular orbit in the plane normal to  $[100]$  marked by a blue circle at  $M_1/M_2 \approx 44.8$  in Fig. 7.

#### IV. SEMICLASSICAL APPROACH

To reveal the existence of a classical exciton dynamics as described in Sec. III the classical dynamics needs to be connected to the quantum spectra of the crystal. This connection can be established by application of semiclassical periodic orbit theory [2, 3, 33]. In these theories, the semiclassical density of states

$$\varrho_{\text{sc}}(E) = \varrho_0(E) + \sum_{\text{po}} \mathcal{A}_{\text{po}} \cos\left(S_{\text{po}}(E)/\hbar - \frac{\pi}{2}\mu_{\text{po}}\right) \quad (23)$$

is given as the sum of the average density of states  $\varrho_0(E)$  and a superposition of fluctuations. The frequencies of the sinusoidal fluctuations depend on the classical action  $S_{\text{po}}$  of the periodic orbits, the amplitudes  $\mathcal{A}_{\text{po}}$  are determined by their stability properties, and the Maslov indices  $\mu_{\text{po}}$  rely on their topology. Since in the semiclassical

limit the periodic orbit formulas coincide with the quantum mechanical result, this approach allows for revealing the contributions of classical orbits to the quantum spectra of the system. The expression for the semiclassical amplitudes  $\mathcal{A}_{\text{po}}$  differs for integrable and non-integrable systems, and the two cases have to be treated separately.

#### A. Integrable systems

In an integrable system one can introduce action-angle variables

$$J_i = \frac{1}{2\pi} \oint_{\mathcal{C}_i} \mathbf{p} d\mathbf{r}, \quad \vartheta_i = \omega_i t + \beta_i, \quad (24)$$

which make the corresponding Hamiltonian independent of the angles  $\vartheta_i$ . The action variables  $J_i$  therefore provide a set of constants of motion. When one angle variable goes from  $\beta_i$  to  $\beta_i + 2\pi$  the system follows an independent irreducible path on a torus  $\mathcal{C}_i$  with frequencies

$$\omega_i = \frac{\partial H}{\partial J_i}. \quad (25)$$

If all ratios  $\omega_i/\omega_j$  for the different frequencies on the torus are given by rational numbers the corresponding orbit becomes periodic and can be characterized by a set of integer winding numbers  $M_i$ , which count the number of cycles on each of the tori  $\mathcal{C}_i$  until the orbit returns to its initial position. The periodic orbits are located on resonant tori.

For integrable systems the density of states is given by the Berry-Tabor formula [3, 33]. In two dimensions the periodic orbits of such a system can be characterized by two winding numbers  $M_1$  and  $M_2$  and the density of states can be written as [33]

$$\varrho_{\text{sc}}(E) = \varrho_0(E) + \frac{1}{\pi\hbar} \sum_{\text{po}} \frac{T_{\text{po}}}{\sqrt{\hbar M_2^3 |g_E''|}} \cos\left(S_{\text{po}}/\hbar - \frac{\pi}{2}\mu_{\text{po}} - \frac{\pi}{4}\right). \quad (26)$$

Here, the semiclassical amplitudes depend on the period of the orbit  $T_{\text{po}}$ , the second winding number  $M_2$ , and on the second derivative

$$g_E'' = \frac{d^2 g_E}{dJ_1^2}, \quad (27)$$

of the relation  $J_2 = g_E(J_1)$  between the two action variables.

#### B. Non-integrable systems

When adding a non-integrable perturbation to an integrable system the resonant tori break up leaving behind isolated periodic orbits. The contribution of these orbits

to the density of states is captured in Gutzwiller's famous trace formula [2]

$$\varrho_{\text{sc}}(E) = \varrho_0(E) + \frac{1}{\pi\hbar} \sum_{\text{ppo}} \frac{T_{\text{ppo}}}{\sqrt{|\det(\mathbf{M}_{\text{ppo}} - \mathbf{1})|}} \cos\left(S_{\text{ppo}}/\hbar - \frac{\pi}{2}\mu_{\text{ppo}}\right). \quad (28)$$

In this case, the amplitudes depend on the stability properties of the system provided by the monodromy matrix  $\mathbf{M}_{\text{ppo}}$ , which describes the linear response of the system to perturbations in directions orthogonal to the orbit. The index 'ppo' indicates primitive periodic orbits meaning that only one repetition of the orbit is considered.

### C. Systems with scaling property

The amplitudes in Gutzwiller's trace formula (28) as well as in the Berry-Tabor-formula (26) depend on the energy or even additional parameters like external fields through the orbit parameters. In some systems it is possible to perform a scaling operation in such a way that the classical orbits no longer depend on a scaling parameter

$$w = \frac{1}{\hbar_{\text{eff}}} = \frac{n_{\text{eff}}}{\hbar}. \quad (29)$$

The action

$$S_{\text{ppo}}(w)/\hbar = \tilde{S}_{\text{ppo}} w, \quad (30)$$

then only depends linearly on the scaling parameter  $w$  with the constant scaled action  $\tilde{S}_{\text{ppo}}$ . Examples where such scaling techniques have been applied are billiard systems [34] or the hydrogen atom in a magnetic field [4, 6, 35]. Transforming the semiclassical density of states (23) from energy to  $w$  domain the resulting expression

$$\varrho_{\text{sc}}(w) = \varrho_0(w) + \text{Re} \sum_{\text{ppo}} \mathcal{A}_{\text{ppo}} \exp\left(i\tilde{S}_{\text{ppo}} w\right), \quad (31)$$

can be understood as a Fourier series with constant periodic orbit parameters. For convenience the Maslov index  $\mu_{\text{ppo}}$  is contained in a complex valued amplitude  $\mathcal{A}_{\text{ppo}}$ .

The individual periodic orbits provide sinusoidal fluctuations to the density of states, which cannot be observed directly. However, the contributions of the periodic orbits can be revealed by Fourier transform from  $w$  to the scaled action domain. The obtained recurrence spectra now exhibit delta peaks at scaled actions  $\tilde{S}_{\text{ppo}}$

$$C_{\text{sc}}(\tilde{S}) = \sum_{\text{ppo}} \mathcal{A}_{\text{ppo}} \delta(\tilde{S} - \tilde{S}_{\text{ppo}}), \quad (32)$$

which allows for a direct assignment of individual orbits to the quantum mechanical recurrence spectrum.

### D. Scaling technique for excitons in cuprous oxide

Here we apply the scaling technique to the classical exciton orbits in cuprous oxide. For all bound states of a hydrogenlike Rydberg spectrum the scaling property (9) holds. The corresponding classical orbits are Kepler ellipses, and thus the classical phase space structure does not depend on the energy of the Rydberg states. However, the classical dynamics underlying a given exciton state depends on the energy. This can be seen when applying the scaling (9) to the Hamiltonian (1). After multiplying by  $n_{\text{eff}}^2$  the Hamiltonian reads

$$H = H_{\text{kin}}(\tilde{\mathbf{p}}, \hat{\mathbf{I}}, \hat{\mathbf{S}}_h) + n_{\text{eff}}^2 H_{\text{SO}}(\hat{\mathbf{I}}, \hat{\mathbf{S}}_h) - \frac{e^2}{4\pi\epsilon_0\epsilon|\tilde{\mathbf{r}}|}. \quad (33)$$

Thus, the impact of the spin-orbit coupling on the states varies with energy. This dependence can be avoided by application of a scaling technique to the spin-orbit coupling. We apply a scaling technique to the spin-orbit term  $H_{\text{SO}}$  by replacing the coupling constant  $\Delta$  in Eq. (7) with an energy-dependent coupling parameter  $\tilde{\Delta}$ , i.e.,

$$\Delta \rightarrow \tilde{\Delta} = \frac{n_0^2}{n_{\text{eff}}^2} \Delta, \quad (34)$$

where the constant parameter  $n_0$  describes the strength of the scaled spin-orbit coupling. While changing material parameters as in Eq. (34) is not directly possible in an experiment, it can prove useful in theoretical investigations. A tunable spin-orbit coupling  $\Delta$  has already been used to study the exchange interaction in the yellow exciton series [25].

### E. Calculation of the trace formula amplitudes

Due to the energy surface  $W_1(\mathbf{p})$  the dynamics of the excitons in cuprous oxide is not integrable. For such systems the density of states is given by Gutzwiller's trace formula (28). Applying the scaling technique for the spin-orbit coupling (34) the amplitudes in Gutzwiller's trace formula read

$$|\mathcal{A}_{\text{ppo}}| = \frac{1}{\pi\hbar} \frac{\tilde{S}_{\text{ppo}}}{\sqrt{|(\lambda_{\perp} + 1/\lambda_{\perp} - 2)(\lambda_{\parallel} + 1/\lambda_{\parallel} - 2)|}}. \quad (35)$$

Note that in the scaled system the period  $T_{\text{ppo}}$  must be replaced by the scaled action  $\tilde{S}_{\text{ppo}}$  [6]. For the isolated nearly circular orbits the stability eigenvalues  $\lambda_{\perp}$  and  $\lambda_{\parallel}$  differ from one, and Eq. (35) can be directly evaluated. The periodic orbit parameters and amplitudes for one cycle of these orbits with  $n_0 = 3, 5, \text{ and } 10$  are given in Table II.

For the calculation of the amplitudes of the two- and three-dimensional orbits Eq. (35), however, is not applicable since the majority of orbits exhibit eigenvalue pairs close to  $\lambda = 1$ , which would lead to the divergence of the

TABLE II. Periodic orbit parameters and Gutzwiller amplitudes for the nearly circular orbits in the planes  $\perp$  to  $[100]$  and  $[1\bar{1}0]$ .

$n_0$	plane	$\tilde{S}_{\text{po}}/(2\pi)$	$\lambda_{\perp} + 1/\lambda_{\perp}$	$\lambda_{\parallel} + 1/\lambda_{\parallel}$	$ \mathcal{A}_{\text{po}} $
3	$[100]$	1.0086	1.8333	1.9295	18.6128
3	$[1\bar{1}0]$	1.0033	2.0338	1.9299	41.2599
5	$[100]$	0.9983	1.9803	1.9917	157.0315
5	$[1\bar{1}0]$	0.9965	2.0041	1.9917	343.0293
10	$[100]$	0.9942	1.9988	1.9995	2619.0137
10	$[1\bar{1}0]$	0.9938	2.0002	1.9995	5671.3482

amplitude. For many orbits we find one eigenvalue pair with  $\lambda$  (and thus  $1/\lambda$ ) close to one. The corresponding degree of freedom can be handled by application of the Berry-Tabor formula (26). The second eigenvalue pair  $\lambda_{\text{po}}$  significantly differs from  $\lambda_{\text{po}} = 1$ , and here the corresponding degree of freedom can be handled by application of Gutzwiller's trace formula (28). When combining the two semiclassical expressions we arrive at the semiclassical amplitude

$$|\mathcal{A}_{\text{po}}| = \frac{1}{\pi\hbar} \frac{1}{\sqrt{|\lambda_{\text{po}} + 1/\lambda_{\text{po}} - 2|}} \frac{\tilde{S}_{\text{po}}}{\sqrt{\hbar M_2^3 |g_E''|}}. \quad (36)$$

The calculation of the semiclassical amplitudes (36) requires the knowledge of the function  $g_E''$  discussed in Sec. IV A. For the two-dimensional orbits the action variables  $J_1$  and  $J_2$  defining the function  $J_2 = g_E(J_1)$  are constructed with the help of derivatives of the classical action

$$S_M = 2\pi(M_1 J_1 + M_2 J_2), \quad (37)$$

with respect to the respective winding number  $M_i$ . The derivatives are obtained numerically via difference quotients of periodic orbits with consecutive winding numbers. For the three-dimensional orbits an effective two-dimensional description can be obtained by combining the contributions of the secular motion in  $\varphi$ - and  $\vartheta$ -direction described by the greatest common divisor  $\tilde{M}_2 = \text{GCD}(M_2, M_3)$  giving the action variable  $\tilde{J}_2 = (M_2/\tilde{M}_2)J_2 + (M_3/\tilde{M}_2)J_3$ . With the two action variables at hand the function  $g_E''$  is obtained with Eq. (27) by differentiating  $J_2$  two times with respect to  $J_1$ . In Fig. 8 this is illustrated for the two-dimensional orbits in the plane normal to  $[100]$  at  $n_0 = 3, 5$ , and 10. The periodic orbit parameters and semiclassical amplitudes of some of these periodic orbits with  $n_0 = 5$  and winding number  $M_2 = 1$  are given in Table III.

## V. VERIFICATION OF EXCITON ORBITS IN QUANTUM SPECTRA

Exciton spectra described by the Hamiltonian (5) have already been investigated experimentally [15] and theoretically [12, 13, 36]. Here, we want to reveal the existence of classical exciton orbits in quantum spectra of the

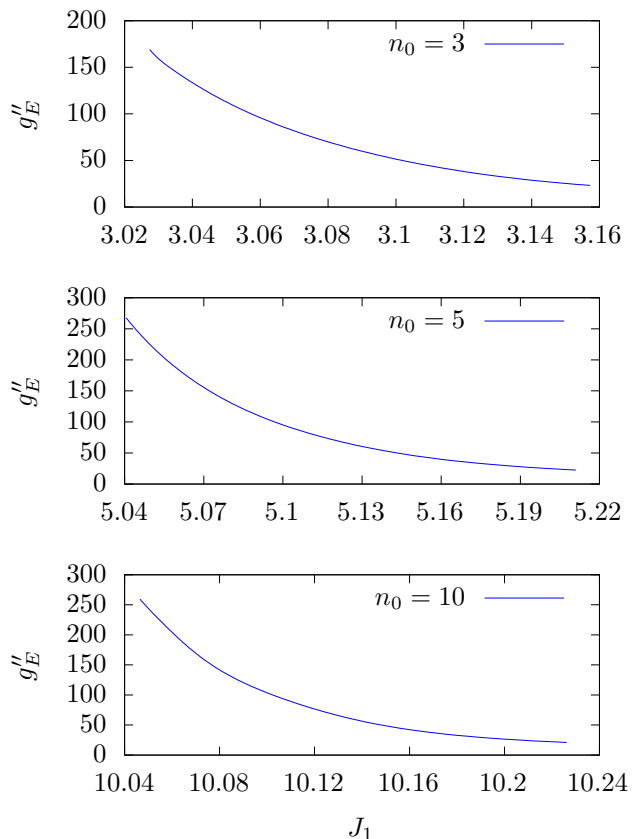


FIG. 8. Second derivative of the function  $J_2 = g_E(J_1)$  with respect to  $J_1$  for the two-dimensional orbits in the plane normal to  $[100]$  at  $n_0 = 3$  (top), 5 (middle), and 10 (bottom). The function of  $g_E''$  for  $n_0 = 5$  has already been presented in the Supplemental Material of Ref. [20].

yellow exciton series of cuprous oxide. For this aim we now exploit the scaling property introduced in Sec. IV by using the scaled spin-orbit splitting (34) in quantum computations. The semiclassical analysis of Fourier transform quantum recurrence spectra then allows for the observation of signatures of classical exciton orbits and a detailed study of the energy dependence of the exciton dynamics in the quantum spectra.

### A. Scaled exciton spectra

For the quantum mechanical description of the scaled system obtained by replacing the spin-orbit coupling in Eq. (33) with the scaled version (34) we need to find the expression for the operators in the scaled coordinates (9). In quantum mechanics the components of coordinates and momenta must satisfy the canonical commutation relations

$$[\hat{r}_i, \hat{p}_j] = i\hbar\delta_{ij}. \quad (38)$$

TABLE III. Periodic orbit parameters and amplitudes of selected two-dimensional orbits in the plane normal to [100] with  $M_2 = 1$  at  $n_0 = 5$ . The flag s/u denotes the stable or unstable partner orbit. For  $M_1 > 12$  the parameters of the stable and unstable orbit are numerically identical.

$M_1$	s/u	$\tilde{S}_{\text{po}}/(2\pi)$	$\lambda_{\perp} + \lambda_{\perp}^{-1}$	$g''_E$	$ \mathcal{A}_{\text{po}} $
5	s	5.592 640	0.361	22.627	1.659
5	u	5.592 664	0.364	22.627	1.659
6	s	6.630 923	-0.862	33.283	1.241
6	u	6.631 008	-0.877	33.283	1.241
7	s	7.663 179	-1.770	46.191	1.072
7	u	7.663 179	-1.773	46.191	1.072
8	s	8.690 824	-1.988	60.435	1.042
8	u	8.691 180	-1.989	60.435	1.042
9	s	9.715 495	-1.971	75.354	1.052
9	u	9.715 495	-1.970	75.354	1.052
10	s	10.737 310	-1.827	90.875	1.084
10	u	10.737 310	-1.827	90.875	1.084
11	s	11.756 909	-1.612	106.562	1.133
11	u	11.756 909	-1.612	106.562	1.133
12	s	12.774 618	-1.347	122.214	1.199
12	u	12.774 623	-1.347	122.214	1.199
13	s,u	13.790 694	-1.047	138.635	1.278
14	s,u	14.805 326	-0.723	155.795	1.374
15	s,u	15.818 674	-0.386	173.523	1.490
16	s,u	16.830 868	-0.044	191.687	1.633

Inserting the scaled variables (9) into Eq. (38) yields the commutation relations

$$[\hat{r}_i, \hat{p}_j] = i \frac{\hbar}{n_{\text{eff}}} \delta_{ij}, \quad (39)$$

in the scaled coordinates, where now the Planck constant is replaced by an effective Planck constant

$$\hbar_{\text{eff}} = \hbar/n_{\text{eff}}. \quad (40)$$

The operators in coordinate space then take the form

$$\hat{\mathbf{r}} = \tilde{\mathbf{r}}, \quad \hat{\mathbf{p}} = -i\hbar_{\text{eff}} \nabla_{\tilde{\mathbf{r}}}. \quad (41)$$

In the scaled picture the Schrödinger equation can now be transformed to the generalized eigenvalue problem

$$\begin{aligned} & \left[ \frac{e^2}{4\pi\epsilon_0\epsilon|\tilde{\mathbf{r}}|} - n_0^2 H_{\text{SO}}(\hat{\mathbf{I}}, \hat{\mathbf{S}}_{\text{h}}) - E_{\text{Ryd}} \right] |\Psi\rangle \\ & = \frac{\hbar^2}{n_{\text{eff}}^2} H_{\text{kin}}(-i\nabla_{\tilde{\mathbf{r}}}, \hat{\mathbf{I}}, \hat{\mathbf{S}}_{\text{h}}) |\Psi\rangle \end{aligned} \quad (42)$$

for the effective Planck constant  $\hbar_{\text{eff}} = \hbar/n_{\text{eff}}$  (or the effective quantum number  $n_{\text{eff}}$ ). The classical dynamics does not depend on the Planck constant, which means that for a given  $n_0$  the classical dynamics is the same for all eigenvalues  $n_{\text{eff},i}$ . This allows us to reveal contributions of the classical exciton dynamics to the quantum mechanical recurrence spectra obtained via Fourier transform of the scaled exciton spectra.

### 1. Matrix representation of the scaled generalized eigenvalue problem

To obtain the quantum mechanical scaled exciton spectra we need to solve the scaled Schrödinger equation (42). To this end we use a complete set of basis functions, which, in addition to the coordinate wave function, also needs to incorporate the quasispin  $\mathbf{I}$  and hole spin  $\mathbf{S}_{\text{h}}$  degrees of freedom.

Our ansatz for the angular part of the basis states is as follows. We first couple the quasispin  $\mathbf{I}$  and the hole spin  $\mathbf{S}_{\text{h}}$  to the effective hole spin  $\mathbf{J}$ . This is an approximate quantum number near the  $\Gamma$  point of the crystal, differentiating between the yellow  $J = 1/2$  and green  $J = 3/2$  states. In a second step,  $\mathbf{J}$  is combined with the orbital angular momentum  $\mathbf{L}$  to form the total angular momentum  $\mathbf{F}$ . Without central-cell corrections the electron spin is a good quantum number of the Hamiltonian and need not be included into our basis. This makes our coupling scheme slightly different compared to previous work [12, 13]. As a complete and discrete set of the radial basis functions, we use the Coulomb-Sturmian functions [37, 38]

$$U_{NL}(\rho) = N_{NL}(2\rho)^L e^{-\rho} L_N^{2L+1}(2\rho), \quad (43)$$

with the radial quantum number  $N$  and the dilated radius  $\rho = r/\alpha$ . The parameter  $\alpha$  can be used to optimize the convergence properties of the basis. With the projection  $M_F$  of the total angular momentum  $\mathbf{F}$  onto the  $z$  axis, we obtain the basis states  $|\Pi\rangle = |N, L, J, F, M_F\rangle$ . When expanding the exciton wave function  $|\Psi\rangle$  as

$$|\Psi\rangle = \sum_{\Pi} c_{\Pi} |\Pi\rangle, \quad (44)$$

the scaled Schrödinger equation (42) can be expressed as a generalized matrix eigenvalue problem,

$$\mathbf{A}\mathbf{c} = \lambda\mathbf{B}\mathbf{c}, \quad (45)$$

with the matrices

$$\mathbf{A}_{\Pi'\Pi} = \langle \Pi' | \frac{e^2}{4\pi\epsilon_0\epsilon|\tilde{\mathbf{r}}|} - n_0^2 H_{\text{SO}}(\hat{\mathbf{I}}, \hat{\mathbf{S}}_{\text{h}}) - E_{\text{Ryd}} | \Pi \rangle, \quad (46)$$

$$\mathbf{B}_{\Pi'\Pi} = \langle \Pi' | H_{\text{kin}}(-i\nabla_{\tilde{\mathbf{r}}}, \hat{\mathbf{I}}, \hat{\mathbf{S}}_{\text{h}}) | \Pi \rangle, \quad (47)$$

and the vector  $\mathbf{c}$  containing the coefficients  $c_{\Pi}$ . The generalized eigenvalue problem (45) can be solved numerically by using a LAPACK routine [39] and a finite number of basis states to obtain a limited number of converged eigenvalues  $\lambda_i = \hbar^2/n_{\text{eff},i}^2$ , and thus a spectrum with discrete values  $n_{\text{eff},i}$  of the effective quantum number. The Hamiltonian (5) is symmetric under operations of the cubic group  $O_{\text{h}}$ . In particular, this includes a fourfold rotational symmetry around the  $z$  axis, which coincides with our chosen quantization axis. Because of this, the matrices (46) and (47) have a block diagonal form. There

are four blocks, which are characterized by the magnetic quantum number  $M_F$  modulo 4 taking the values  $1/2$ ,  $3/2$ ,  $5/2$ , and  $7/2$ , respectively. Each of these blocks additionally splits into two blocks characterized by their parity. We exploit this block structure to accelerate the numerical calculations.

## 2. Quantum recurrence spectra

We now want to uncover the contributions of classical orbits directly in the scaled quantum spectra

$$\varrho(n_{\text{eff}}) = \sum_i \delta(n_{\text{eff}} - n_{\text{eff},i}). \quad (48)$$

The eigenvalues of the scaled Schrödinger equation (42) are shown in Fig. 9 for  $n_0 = 3, 5$ , and  $10$ , where  $n_0$  parameterizes the scaled classical dynamics, as shown in the PSOS in Fig. 2, i.e., spectra with increasing  $n_0$  are related to a classical exciton dynamics with slower secular motion of orbits. The lowest axis label in Fig. 9 gives the eigenvalues  $n_{\text{eff}}$  and the upper labels of the individual plots compare the scaled spin-orbit coupling  $\tilde{\Delta}$  to the real physical value  $\Delta$ , i.e.,  $\tilde{\Delta}/\Delta = 1$  belongs to the crystal with the real (unscaled) material parameters of cuprous oxide.

As outlined in Sec. IV the scaled density of states (48) can be approximated by a superposition of sinusoidal fluctuations, whose amplitudes and frequencies are directly related to properties of the periodic orbits of the underlying classical dynamics. Thus, we analyze the fluctuations of the scaled quantum spectrum (48) via Fourier transform in the variable  $n_{\text{eff}}$ , i.e., a quantum recurrence spectrum is obtained as

$$C(S) = \frac{1}{2\pi} \int \varrho(n_{\text{eff}}) e^{-i\tilde{S}n_{\text{eff}}/\hbar} dn_{\text{eff}}. \quad (49)$$

The quantum recurrence spectrum (49) should provide peaks at frequencies given by the scaled actions  $\tilde{S}_{\text{po}}$  of the periodic orbits of the associated classical exciton dynamics. Due to the finite number of converged states obtained from numerically solving the generalized eigenvalue problem (42) the peaks appear broadened in comparison to the full (infinite) spectrum. This can also be understood in the following way. The finite spectrum can be obtained by multiplying the infinite one with a rectangular window function. Fourier transforming this expression will give the convolution of the delta peaks of the Fourier transformed infinite spectrum and

$$\frac{\sin\left(\Delta n_{\text{eff}} \tilde{S}_{\text{po}} / (2\hbar)\right)}{\pi \tilde{S}_{\text{po}} / \hbar} e^{-in_{\text{eff}}^0 \tilde{S}_{\text{po}} / \hbar}, \quad (50)$$

with the length of the finite spectrum  $\Delta n_{\text{eff}}$  and its center  $n_{\text{eff}}^0$ . In addition to the main peaks this will also lead

to the appearance of side peaks. To suppress these unwanted features we use a Gaussian window function

$$w(n_{\text{eff}}) \equiv \exp\left(-\frac{(n_{\text{eff}} - n_{\text{eff}}^0)^2}{2\sigma^2}\right), \quad (51)$$

where we choose  $\sigma \approx \Delta n_{\text{eff}}/6$ . The resulting expression for the quantum mechanical recurrence spectrum is given by

$$\begin{aligned} \hat{C}(\tilde{S}) &= \frac{1}{2\pi} \sum_{k=1}^{k_{\text{max}}} \int w(n_{\text{eff}}) \delta(n_{\text{eff}} - n_{\text{eff},k}) e^{-in_{\text{eff}} \tilde{S} / \hbar} dn_{\text{eff}} \\ &= \frac{1}{2\pi} \sum_{k=1}^{k_{\text{max}}} w(n_{\text{eff},k}) \left[ \cos\left(n_{\text{eff},k} \tilde{S} / \hbar\right) - i \sin\left(n_{\text{eff},k} \tilde{S} / \hbar\right) \right], \end{aligned} \quad (52)$$

where  $k_{\text{max}}$  is the number of converged eigenvalues  $n_{\text{eff},k}$  considered.

## 3. Semiclassical analysis and discussion

The quantum recurrence spectra obtained from the spectra in Fig. 9 are shown as solid black lines in Fig. 10 for the three different values of  $n_0$ . They exhibit distinct peaks at certain values of the scaled action  $\tilde{S}/(2\pi)$ . The number of peaks and thus the complexity of the quantum recurrence spectra increases with decreasing values of  $n_0$ , i.e., with decreasing energy of the excitons. The observed structures in the quantum recurrence spectra can be explained and interpreted with the help of the periodic exciton orbits. The semiclassical amplitudes of periodic orbits at positions  $\tilde{S}_{\text{po}}$  are shown in Fig. 10 as colored bars, labeled by the winding numbers of the corresponding orbits. The majority of the peaks in the quantum recurrence spectra can be understood in terms of classical orbits. For low actions  $\tilde{S}/(2\pi)$  all peaks in the recurrence spectra can be assigned to the nearly circular orbits, which appear as central fixed point in the two symmetry planes in Fig. 2. These orbits move on one-dimensional tori and can therefore be labeled by an integer winding number  $M_1$  which characterizes the repetitions of the orbits.

For increasing actions longer two-dimensional and three-dimensional orbits start to contribute to the recurrence spectra, leading to an increased density of peaks. These orbits belong to motion on two-dimensional tori in the two symmetry planes characterized by winding numbers  $M_1:M_2$  or motion on fully three-dimensional tori characterized by winding numbers  $M_1:M_2:M_3$ . Orbits with the same winding numbers  $M_1:M_2$  appear clustered together in the recurrence spectra in Fig. 10. Therein orbits in the mostly stable symmetry plane normal to  $[100]$  exhibit the highest action as well as semiclassical amplitudes. The orbits in the unstable symmetry plane normal to  $[1\bar{1}0]$  have the lowest action in the cluster and

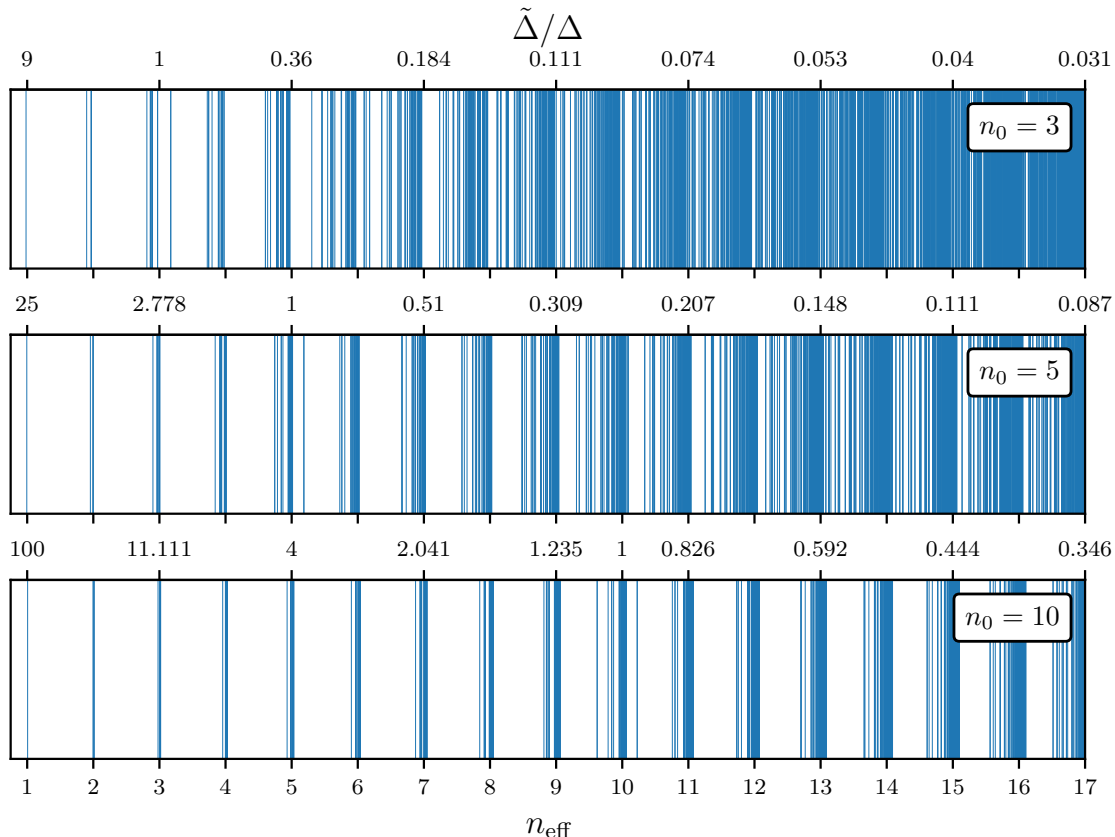


FIG. 9. Eigenvalue spectra for  $n_0 = 3$  (top),  $n_0 = 5$  (middle), and  $n_0 = 10$  (bottom). Each eigenvalue contributes a delta peak to the quantum mechanical density of states (48). The lowest axis label for the effective quantum number  $n_{\text{eff}}$  is valid for all three parts of the figure. The three upper labels for the ratio  $\tilde{\Delta}/\Delta$  of the scaled and real physical spin-orbit coupling are valid for the corresponding individual plots. Part of the spectrum for  $n_0 = 5$  has already been presented in Ref. [20].

typically also the lowest semiclassical amplitude. At intermediate actions the three-dimensional orbits can be found.

For  $n_0 = 3$  only two pairs of primitive three-dimensional orbits (not counting repetitions) are found in the presented action range. Due to their small number the value  $g_E''$  for the corresponding orbits in the plane normal to  $[100]$  are used for the calculation of their semiclassical amplitudes at  $n_0 = 3$ . This should provide a good approximation since the action of these orbits approaches their two-dimensional counterpart. Again, their  $M_1:M_2$  values correspond to the region in which a change in stability properties can be observed in Fig. 6 (top). For  $n_0 = 5$  multiple three-dimensional orbits exist in the given range, whereas for  $n_0 = 10$  the three-dimensional orbits start to appear only at higher actions. For increasing  $n_0$  the contributions of the two- and three-dimensional orbits decrease at low actions  $\tilde{S}/(2\pi)$  compared to the one-dimensional orbits. On the one hand the relative amplitudes of orbits with the same winding numbers decrease for increasing  $n_0$ . On the other hand the range of  $M_1:M_2$  values increases with  $n_0$  yielding more contributions for higher actions  $\tilde{S}/(2\pi)$ . The

maximum value  $(M_1/M_2)_{\text{max}}$  is reached at the nearly circular one-dimensional orbits. Since  $(M_1/M_2)_{\text{max}}$  increases for increasing  $n_0$  the secular motion slows down in the neighborhood of the central elliptical fixed points giving a more hydrogenlike behavior in this region. This also becomes apparent in the recurrence spectra. In the hydrogenlike case only Kepler ellipses with scaled action  $\tilde{S}_{\text{po}}/(2\pi) = n$  with  $n = 1, 2, \dots$  exist and therefore the peaks in the corresponding recurrence spectrum are located at the integers giving the number of repetitions of the orbits. When introducing the energy surface for the yellow series  $W_1$  only the nearly circular orbits in the symmetry planes are periodic after one cycle providing a similar contribution like the Kepler ellipses in the hydrogenlike case. In comparison, contributions of other two-dimensional orbits in the symmetry planes and three-dimensional orbits become important for larger values of  $\tilde{S}/(2\pi)$ . With increasing values of  $n_0$  this effect becomes more prominent and leads to a more hydrogenlike appearance of the recurrence spectra at  $n_0 = 5$  and  $10$  in Fig. 10. This trend can also be observed at higher values of  $n_0$ .

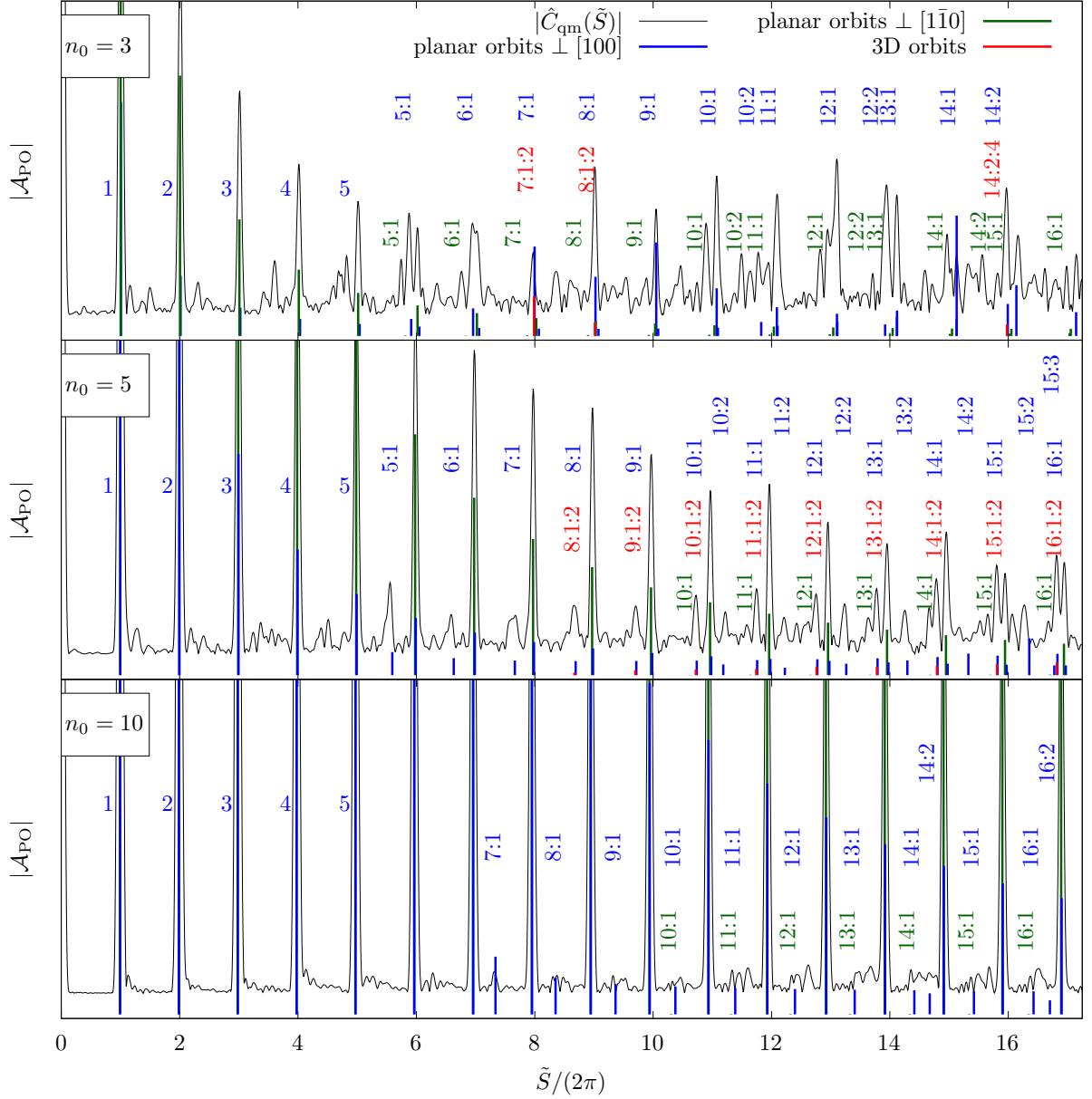


FIG. 10. Recurrence spectra for  $n_0 = 3$  (top),  $n_0 = 5$  (middle), and  $n_0 = 10$  (bottom). The semiclassical amplitudes are shown as colored bars. Amplitudes for orbits in the plane normal to  $[100]$  are shown in blue, amplitudes for orbits in the plane normal to  $[1\bar{1}0]$  in green and amplitudes for three-dimensional orbits are shown in red. The amplitudes are labeled with the winding numbers of the corresponding orbits. The quantum recurrence spectra (black line) are shifted upwards for better visibility. The semiclassical amplitudes and their coupling are valid for the corresponding individual plots. The recurrence spectrum for  $n_0 = 5$  has already been shown in Ref. [20].

## VI. CONCLUSION AND OUTLOOK

In this paper we investigated the classical dynamics of the yellow excitons in cuprous oxide and the contributions of classical periodic exciton orbits to the quantum spectra at various energies. This was achieved by applying the scaling technique for the spin-orbit coupling introduced in Ref. [20]. For the two distinct symmetry planes normal to the  $[100]$  axis and the  $[1\bar{1}0]$  axis the PSOS

revealed the phase space structure, viz. the existence of a central fixed point surrounded by near-integrable tori and a small chaotic region. The secular motion of orbits around the central fixed points becomes slower and the size of the chaotic regions decreases with increasing energy. In accordance with the Poincaré-Birkhoff theorem periodic orbits on the near-integrable tori exist in pairs and can be labeled by two integer winding numbers  $M_1:M_2$ . Out of the symmetry planes fully three-

dimensional orbits on resonant tori characterized by three winding numbers  $M_1:M_2:M_3$  do exist.

The existence of classical periodic exciton orbits has been verified directly in quantum mechanical exciton spectra. The obtained results go significantly beyond those presented in Ref. [20], where the analysis has been restricted to a single energy value with  $n_0 = 5$ . Here, we have extended our analysis to different energies and discussed the energy dependence of the classical exciton dynamics and the corresponding recurrence spectra by way of examples at  $n_0 = 3, 5$ , and 10. The Fourier transform quantum recurrence spectra show detailed structures of peaks located at distinct values of the scaled action. Their occurrence can both qualitatively and quantitatively be explained in terms of periodic exciton orbits by application of trace formulas from semiclassical periodic orbit theories [2, 3, 40]. Line by line comparisons reveal a good agreement between semiclassical and quantum mechanical recurrence spectra at various energies. The recurrence spectra show an increasing complexity with decreasing energy, where two- and three-dimensional periodic orbits occur at lower values of the scaled action and with increased amplitudes compared to the nearly circular orbits. We thus observe significant deviations from a purely hydrogenlike system where the Kepler ellipses and their repetitions would provide peaks only at multiples of  $\tilde{S} = 2\pi$ . This is related to a growing influence of the spin-orbit interaction in the cuprous oxide semiconductor and thus an increasing velocity of the secular motion of the exciton orbits compared to hydrogenlike Keplerian orbits.

In this paper we have focused on exciton spectra and

the classical exciton dynamics related to the yellow exciton series in cuprous oxide. In future work it would be interesting to further investigate the classical dynamics of excitons in cuprous oxide, including the green exciton series [36]. The PSOS are only capable of presenting the phase space of a two-dimensional system and are therefore not suited to study the phase space of excitons when including three-dimensional motion. One approach to study the corresponding dynamics could be using Lagrangian descriptors [41–43], which have proven to be a useful tool for revealing phase structures in non-integrable systems.

Another interesting topic would be to extend the semiclassical treatment. In this work the contributions of classical orbits were studied by connecting classical orbits to the peaks in the quantum recurrence spectra. Due to the large regular part of phase space and the possibility of reconstructing action variables from the classical orbits, it will be interesting to see if the spectrum of excitons in cuprous oxide can be directly connected to classical orbits using the EBK-quantization method [44]. These approaches have successfully been applied for the hydrogen atom in external electric and magnetic fields [31, 32]. This would allow for a direct understanding of the quantum spectra in terms of classical exciton orbits.

## ACKNOWLEDGMENTS

This work was supported by Deutsche Forschungsgemeinschaft (DFG) through Grant No. MA1639/16-1.

- 
- [1] A. Sommerfeld, Zur Quantentheorie der Spektrallinien, *Annalen der Physik* **356**, 1 (1916).
  - [2] M. C. Gutzwiller, *Chaos in Classical and Quantum Mechanics* (Springer, New York, 1990).
  - [3] M. V. Berry and M. Tabor, Closed orbits and the regular bound spectrum, *Proc. R. Soc. Lond. A* **349**, 101 (1976).
  - [4] H. Friedrich and H. Wintgen, The hydrogen atom in a uniform magnetic field – An example of chaos, *Physics Reports* **183**, 37–79 (1989).
  - [5] H. Hasegawa, M. Robnik, and G. Wunner, Classical and Quantal Chaos in the Diamagnetic Kepler Problem, *Progress of Theoretical Physics Supplement* **98**, 198 (1989).
  - [6] J. Main, Use of harmonic inversion techniques in semiclassical quantization and analysis of quantum spectra, *Phys. Rep.* **316**, 233–338 (1999).
  - [7] G. S. Ezra, K. Richter, G. Tanner, and D. Wintgen, Semiclassical cycle expansion for the helium atom, *Journal of Physics B: Atomic, Molecular and Optical Physics* **24**, L413 (1991).
  - [8] F. Haake, S. Gnutzmann, and M. Kuš, *Quantum Signatures of Chaos, Fourth Edition*, Springer Series in Synergetics (Springer, Cham, 2018).
  - [9] F. Schöne, S.-O. Krüger, P. Grünwald, M. Aßmann, J. Heckötter, J. Thewes, H. Stolz, D. Fröhlich, M. Bayer, and S. Scheel, Coupled valence band dispersions and the quantum defect of excitons in Cu<sub>2</sub>O, *Journal of Physics B: Atomic, Molecular and Optical Physics* **49**, 134003 (2016).
  - [10] F. Schöne, S.-O. Krüger, P. Grünwald, H. Stolz, S. Scheel, M. Aßmann, J. Heckötter, J. Thewes, D. Fröhlich, and M. Bayer, Deviations of the exciton level spectrum in Cu<sub>2</sub>O from the hydrogen series, *Phys. Rev. B* **93**, 075203 (2016).
  - [11] J. Thewes, J. Heckötter, T. Kazimierzczuk, M. Aßmann, D. Fröhlich, M. Bayer, M. A. Semina, and M. M. Glazov, Observation of high angular momentum excitons in cuprous oxide, *Phys. Rev. Lett.* **115**, 027402 (2015).
  - [12] F. Schweiner, J. Main, M. Feldmaier, G. Wunner, and C. Uihlein, Impact of the valence band structure of Cu<sub>2</sub>O on excitonic spectra, *Phys. Rev. B* **93**, 195203 (2016).
  - [13] F. Schweiner, J. Main, G. Wunner, and C. Uihlein, Even exciton series in Cu<sub>2</sub>O, *Phys. Rev. B* **95**, 195201 (2017).
  - [14] E. F. Gross, Optical spectrum of excitons in the crystal lattice, *Il Nuovo Cimento* (1955-1965) **3**, 672 (1956).

- [15] T. Kazimierzczuk, D. Fröhlich, S. Scheel, H. Stolz, and M. Bayer, Giant Rydberg excitons in the copper oxide  $\text{Cu}_2\text{O}$ , *Nature* **514**, 343 (2014).
- [16] M. A. M. Versteegh, S. Steinhauer, J. Bajo, T. Lettner, A. Soro, A. Romanova, S. Gyger, L. Schweickert, A. Mysyrowicz, and V. Zwiller, Giant Rydberg excitons in  $\text{Cu}_2\text{O}$  probed by photoluminescence excitation spectroscopy, *Phys. Rev. B* **104**, 245206 (2021).
- [17] N. O. Lipari and M. Altarelli, Theory of indirect excitons in semiconductors, *Phys. Rev. B* **15**, 4883 (1977).
- [18] C. Uihlein, D. Fröhlich, and R. Kenklies, Investigation of exciton fine structure in  $\text{Cu}_2\text{O}$ , *Phys. Rev. B* **23**, 2731 (1981).
- [19] J. Ertl, P. Rommel, M. Mom, J. Main, and M. Bayer, Classical and semiclassical description of Rydberg excitons in cuprous oxide, *Phys. Rev. B* **101**, 241201(R) (2020).
- [20] J. Ertl, M. Marquardt, M. Schumacher, P. Rommel, J. Main, and M. Bayer, Signatures of exciton orbits in quantum mechanical recurrence spectra of  $\text{Cu}_2\text{O}$ , *Phys. Rev. Lett.* **129**, 067401 (2022).
- [21] G. Koster, J. Dimmock, R. Wheeler, and H. Statz, *Properties of the thirty-two point groups*, Massachusetts Institute of Technology Press research monograph (M.I.T. Press, Cambridge, 1963).
- [22] J. M. Luttinger and W. Kohn, Motion of electrons and holes in perturbed periodic fields, *Phys. Rev.* **97**, 869 (1955).
- [23] J. M. Luttinger, Quantum theory of cyclotron resonance in semiconductors: General theory, *Phys. Rev.* **102**, 1030 (1956).
- [24] K. Suzuki and J. C. Hensel, Quantum resonances in the valence bands of germanium. I. Theoretical considerations, *Phys. Rev. B* **9**, 4184 (1974).
- [25] P. Rommel, J. Main, A. Farenbruch, D. R. Yakovlev, and M. Bayer, Exchange interaction in the yellow exciton series of cuprous oxide, *Phys. Rev. B* **103**, 075202 (2021).
- [26] J. Heckötter, P. Rommel, J. Main, M. Aßmann, and M. Bayer, Analysis of the fine structure of the D-exciton shell in cuprous oxide, *physica status solidi (RRL)* – Rapid Research Letters **15**, 2100335 (2021).
- [27] P. Schmelcher and L. S. Cederbaum, Regularity and chaos in the center of mass motion of the hydrogen atom in a magnetic field, *Zeitschrift für Physik D Atoms, Molecules and Clusters* **24**, 311 (1992).
- [28] J. W. Hodby, T. E. Jenkins, C. Schwab, H. Tamura, and D. Trivich, Cyclotron resonance of electrons and of holes in cuprous oxide,  $\text{Cu}_2\text{O}$ , *Journal of Physics C: Solid State Physics* **9**, 1429 (1976).
- [29] O. Madelung, U. Rössler, and M. Schulz, eds., *Landolt-Börnstein - Group III Condensed Matter* (Springer-Verlag, Berlin Heidelberg, 1998).
- [30] R. Brankin, I. Gladwell, and L. Shampine, *RKSUITE: a suite of Runge-Kutta codes for the initial value problem for ODEs, Softreport 92-S1* (Department of Mathematics, Southern Methodist University, Dallas, Texas, 1992).
- [31] S. Gekle, J. Main, T. Bartsch, and T. Uzer, Extracting multidimensional phase space topology from periodic orbits, *Phys. Rev. Lett.* **97**, 104101 (2006).
- [32] S. Gekle, J. Main, T. Bartsch, and T. Uzer, Hydrogen atom in crossed electric and magnetic fields: Phase space topology and torus quantization via periodic orbits, *Phys. Rev. A* **75**, 023406 (2007).
- [33] S. Tomsovic, M. Grinberg, and D. Ullmo, Semiclassical trace formulas of near-integrable systems: Resonances, *Phys. Rev. Lett.* **75**, 4346 (1995).
- [34] P. Cvitanović and B. Eckhardt, Periodic-orbit quantization of chaotic systems, *Phys. Rev. Lett.* **63**, 823 (1989).
- [35] A. Holle, J. Main, G. Wiebusch, H. Rottke, and K. H. Welge, Quasi-Landau spectrum of the chaotic diamagnetic hydrogen atom, *Phys. Rev. Lett.* **61**, 161 (1988).
- [36] P. Rommel, P. Zielinski, and J. Main, Green exciton series in cuprous oxide, *Phys. Rev. B* **101**, 075208 (2020).
- [37] J. Zamastil, F. Vinette, and M. Šimánek, Calculation of atomic integrals using commutation relations, *Phys. Rev. A* **75**, 022506 (2007).
- [38] M. A. Caprio, P. Maris, and J. P. Vary, Coulomb-Sturmian basis for the nuclear many-body problem, *Phys. Rev. C* **86**, 034312 (2012).
- [39] R. B. Lehoucq, D. C. Sorensen, and C. Yang, *ARPACK Users' Guide* (Society for Industrial and Applied Mathematics, 1998).
- [40] D. Ullmo, M. Grinberg, and S. Tomsovic, Near-integrable systems: Resonances and semiclassical trace formulas, *Phys. Rev. E* **54**, 136 (1996).
- [41] C. Mendoza and A. M. Mancho, Hidden geometry of ocean flows, *Phys. Rev. Lett.* **105**, 038501 (2010).
- [42] A. M. Mancho, S. Wiggins, J. Curbelo, and C. Mendoza, Lagrangian descriptors: A method for revealing phase space structures of general time dependent dynamical systems, *Communications in Nonlinear Science and Numerical Simulation* **18**, 3530 (2013).
- [43] J. Daquin, R. Pédenon-Orlanducci, M. Agaoglou, G. García-Sánchez, and A. M. Mancho, Global dynamics visualisation from lagrangian descriptors. applications to discrete and continuous systems, *Physica D: Nonlinear Phenomena* **442**, 133520 (2022).
- [44] L. J. Curtis and D. G. Ellis, Use of the Einstein-Brillouin-Keller action quantization, *American Journal of Physics* **72**, 1521 (2004).